Role of Hyaluronic Acid on the Nucleation Kinetics of Calcium Oxalate Hydrates in Artificial Urine Quantified with Droplet Microfluidics

Ibis, F.; Alhaji Nuhu, M.R.; Penha, Frederico Marques ; Yu, T.W.; van der Heijden, A.E.D.M.; Kramer, H.J.M.; Eral, H.B.

DOI
10.1021/acs.cgd.2c00198

Publication date
2022

Document Version
Final published version

Published in
Crystal Growth & Design

Citation (APA)
Ibis, F., Alhaji Nuhu, M. R., Penha, F. M., Yu, T. W., van der Heijden, A. E. D. M., Kramer, H. J. M., & Eral, H. B. (2022). Role of Hyaluronic Acid on the Nucleation Kinetics of Calcium Oxalate Hydrates in Artificial Urine Quantified with Droplet Microfluidics. *Crystal Growth & Design*, *22*(6), 3834-3844. https://doi.org/10.1021/acs.cgd.2c00198

CRYSTAL
GROWTH
&DESIGN

Role of Hyaluronic Acid on the Nucleation Kinetics of Calcium Oxalate Hydrates in Artificial Urine Quantified with Droplet Microfluidics

Fatma Ibis, Manzoor Alhaji Nuhu, Frederico Marques Penha, Tsun Wang Yu,
Antoine E. D. M. van der Heijden, Herman J. M. Kramer, and Huseyin Burak Eral*

Cite This: *Cryst. Growth Des.* 2022, 22, 3834−3844

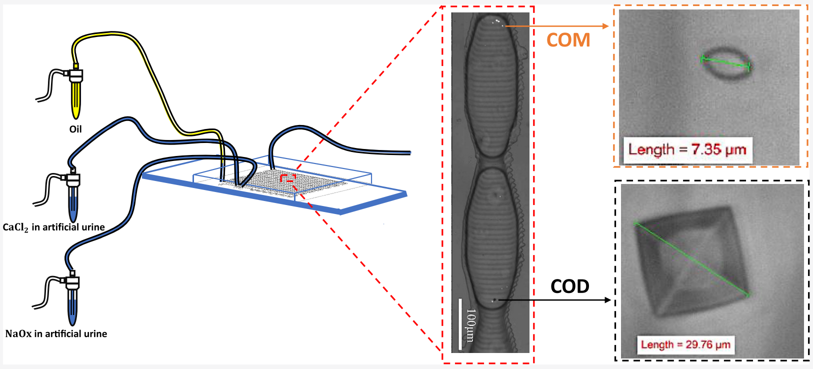

ABSTRACT: The increasing prevalence of urolithiasis in industrialized societies triggered considerable interest in how various species found in urine regulate the nucleation and growth of common kidney stone constituents such as calcium oxalate (CaOx). Yet, the role macromolecules play in kidney stone formation is often overlooked due to their low concentration in urine. In this study, we investigate the nucleation kinetics of CaOx in artificial urine with droplet-based microfluidic induction time measurements at varying concentrations of oxalate and hyaluronic acid (HA), a polysaccharide commonly found in urine. The formation of two pseudo-polymorphic forms of calcium oxalate crystals, calcium oxalate monohydrate (COM) and calcium oxalate dihydrate (COD), are carefully monitored using polarized light microscopy in induction time experiments. COM and COD nucleated concomitantly in artificial urine yet with distinct kinetics. Our results indicate that higher oxalate concentrations favor the formation of COD, the metastable form, over COM, the most stable form. Moreover, COD is also the fastest nucleating form in droplets under studied conditions. Furthermore, increasing the concentration of HA at fixed calcium and oxalate concentrations favored the nucleation of COM. We observed that in droplets where COM nucleated first, COD was not formed within the experimental time scale. However, in the droplets where COD appeared first, COM crystals were also observed later. We hope our findings shed light on the role macromolecules such as HA plays in dictating the pseudo-polymorphic form of CaOx and guide next generation treatments.

INTRODUCTION

Kidney stones contain inorganic crystals merged with organic constituents.[1−3] Formation of kidney stones, also known as urolithiasis, is attributed to a plethora of underlying patient conditions. The frequency of urolithiasis cases varies based on age, sex, genetics, medical history, fluid intake, diet, physical activity, urine pH, and climate.[4−6] It is reported that 7 and 13% of all women and men, respectively, will develop kidney stones in their lifetime.[4,7−10] Kidney stones can be flushed from the urinary system easily, in case their diameter is less than five millimeters.[11] Stones with sizes above seven millimeters are problematic and generally need a urological intervention.[11,12] The obvious question that of interest to both medical scientists and engineers is how kidney stones nucleate in urine in nanoscale then grow to millimeter scale. A complete mechanistic understanding of urolithiasis will inform development of more effective treatments.

Analyses of kidney stones from patients showed three main types of crystals, calcium oxalate, calcium phosphate, and uric acid. Regular human urine is supersaturated with respect to calcium oxalate and calcium phosphate.[13,14] A low urine volume often goes along with high calcium, sodium, oxalate,

Received: February 15, 2022
Revised: April 13, 2022
Published: April 28, 2022

https://doi.org/10.1021/acs.cgd.2c00198

and urate concentrations and can result in a state of supersaturation of the urine solution with respect to the calcium oxalate and calcium phosphate crystals. Such a supersaturated condition is the driving force behind the nucleation of these inorganic crystals and is the first step in the formation of kidney stones.[15] Nearly 80% of stones consist mainly of hydrates of calcium oxalate. Calcium oxalate (CaOx) crystals can be presented as calcium oxalate dihydrate (COD, weddellite) or calcium oxalate monohydrate (COM, whewellite), which is the most common and the most stable form at body temperature (37 °C).[1,16−20] People with a high risk of kidney stones produce urine with a higher supersaturation of CaOx as compared to non-stone formers.[21,22] Hypercalciuria and hyperoxaluria, high levels of calcium and oxalate in the urine, respectively, are two conditions connected to the high frequency of kidney stones. A patient is considered to exhibit hypercalciuria when the amount of calcium in urine reaches values greater than 300 mg/24 h for men and 250 mg/24 h for women.[2,7,23,24] The daily oxalate excretion can vary between 10 and 40 mg per 24 h. The amount of oxalate exceeding 40−45 mg per 24 h is considered as hyperoxaluria.[25−27]

Urine also comprises different types of organic and inorganic substances capable of influencing the formation of CaOx crystals (or stones).[28] These compounds might either facilitate (promoters) or prevent (inhibitors) the stone formation. Stone formation is considered to be inhibited by various inorganic substances such as magnesium and organic substances like nephrocalcin and other organic macromolecules such as hyaluronic acid (HA).[29,30] HA is a negatively charged, high molecular weight polysaccharide found in practically all biological tissues. It is a copolymer of *N*-acetyl-D-glucosamine and D-glucuronic acid.[31] HA is thought to play an important role in binding cations, especially Ca^{2+}, and retaining water.[32] Moreover, overexpressed HA induced by long-term hydrodynamic stress or the impact of stone fragments is long suspected to play a role in kidney stone formation.

The studies of HA expression and CaOx retention in cells have been reported in the literature. Borges *et al.* reported that kidney cells synthesize HA as a protection mechanism from the presence of CaOx crystals and oxalate ions, which was seen to partially affect crystallization kinetics.[33] Gan *et al.* found that the expression of HA was increased during wound healing because of cell injury and also this injury contributes to CaOx adhesion to the cell surface.[34] Asselman *et al.* reported that the expression of HA by injured cells seems to play a role in the retention of CaOx crystals.[35] The effect of HA on CaOx stone formation was evaluated in the presence of additives, such as citrate, as well as various amino acids, dipeptides, and enzymes in solutions with varying pH values.[36,37] However, an in vitro study focusing on how HA influences the kinetics of CaOx crystallization and its pseudo-polymorphic transitions has not been reported in the literature, to the best of our knowledge.

Laboratory experiments in well-mixed vessels are commonly used to investigate CaOx formation in the presence of different additives in water or artificial urine. Xie *et al.* found that the aggregation of amorphous CaOx complexes induced COM stone formation in water.[38] Gardner and Nancollas observed that sodium pyrophosphate exhibited a strong inhibiting effect on COM growth in water.[39] In other studies that used artificial urine as a solvent, Hsu *et al.* investigated the nucleation kinetics of CaOx using a batch crystallizer in the presence of various additives in synthetic urine.[40] Cerini *et al.* worked on nucleation of CaOx in urine with the additive of albumin, leading to COD formation particularly.[41] Polat and Eral characterized CaOx crystals forming in a well-mixed liter size crystallizer in water and artificial urine media.[42] This study reported the emergence of a small fraction of COD crystals in the presence of HA only for aqueous medium, where the control samples with no HA nucleated as COM exclusively.[42] To sum up, a large body of in vitro CaOx crystallization experiments aiming to shed light on the underlying mechanism behind kidney stone formation appeared in literature. These laboratory studies used a broad range of techniques ranging from thermodynamic studies focusing on the properties of the resulting crystal form[43−45] to atomic force microscopy studies monitoring growth and nucleation kinetics[46] have been reported.

Recently, lab on a chip technology has been applied to investigate CaOx crystallization. The driver to implement this technology is the ability to explore a broad range of experimental conditions with minute amounts of solute, a feature most attractive for difficult to synthesize or isolate macromolecules such as proteins. Lattife *et al.* used a microfluidic device to understand CaOx formation by mimicking the conditions for CaOx precipitation in collecting duct kidneys.[47] Gombedza *et al.* investigated effect of melamine on CaOx growth, and they found that melamine induced CaOx formation.[48] In addition to the aforementioned advantages, lab on a chip technology, particularly droplet microfluidics, enables researchers to strictly control length scales for momentum, mass transfer, and heat transport.[49−55] Furthermore, microfluidics enables rapidly scanning a large phase space with a significant number of identical experiments[51,56−59]—a feat deemed laborious and time-intensive batch lab-scale approaches.[60,61] In a microfluidic system, uniformly sized micro-droplets can act as isolated microreactors enabling the realization of a large number of experiments under excellently controlled and identical circumstances. A number of in vitro studies focusing on promoters and inhibitors have been reported[62−65] yet with a wide range of artificial urine formulations.[66−69] The multiplexing ability of microfluidics can facilitate a precise parametric search of the broad range of urine formulations reported and test the validity of observations across different formulations. These advantages may benefit researchers looking to quantify nucleation and growth rates[59,70−72] and compare them to in vivo kidney stone formation rates. Yet, microfluidics comes with its challenges. To mention a few, (i) the micro- to nanoliter droplets offer long induction times due to their small volume and (ii) rapidly mixing droplets at aforementioned volumes is dominated by viscous forces and requires dedicated micromixers.

Each human kidney has around 1.2 million nephrons, which are the smallest structural and functional units of this organ. The nephrons comprise a renal corpuscle, proximal tubule, loop of Henle, distal tubule, and collecting duct system.[73−75] About 10 nephrons give birth to one single collecting duct with a diameter of ca. 100 μm.[47,76] Most kidney stone formation is seen in these collecting ducts. Moreover, the flow rate in these ducts is roughly 10.0 nL/min, showing laminar flow inside the collecting duct.[47,77] The dimensions of our droplets and the microfluidic device are inspired by the dimensions of the collecting duct in a kidney.

Nucleation kinetics can be quantified with a broad list of approaches implemented both in macroscopic vessels[78,79] and microfluidic devices.[80] In a nutshell, the nucleation kinetics in droplet based microfluidic induction time measurements is

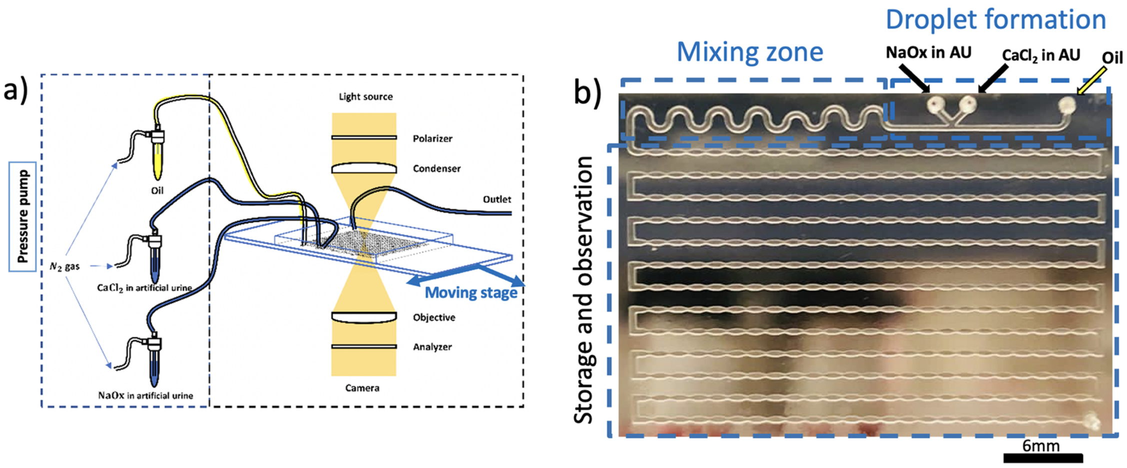

Figure 1. Experimental setup with the microfluidic platform: (a) schematic of the experimental set showing the microfluidic system, the motorized stage, and the polarized light microscopy optics used during induction time measurements. (b) A photo of the complete microfluidic chip showing the "droplet formation" and "mixing" along with "storage and observation" zones on the PDMS microfluidic platform, scale bar 6 mm.

measured by identifying the emergence of the first crystal in a droplet, also known as induction time, for a large number of droplets (>60) in this study. The cumulative fraction of droplets nucleated at a given time after mixing of reactive species, $p(t)$, is fitted with models discussed in detail in Microfluidic Induction Time Measurements to extract characteristic induction time and effective nucleation rate. Microfluidic induction time measurement conducted with polarized light microscopy offers unique advantages. Polarized light microscopy leverages an optical property called birefringence in which the refractive index varies depending on the polarization and the propagation direction of light.[81,82] COM predominantly shows strong birefringence,[83] whereas COD is only slightly birefringent.[66] Polarized light microscopy has previously been used to differentiate calcium oxalate pseudo-polymorphic forms.[84,85] Consequently, implementing polarized light microscopy in microfluidic nucleation kinetics measurement enables us to identify concomitantly nucleating pseudo-polymorphs and transformation kinetics of these pseudo-polymorphs.

In this study, the nucleation kinetics of CaOx at varying concentrations of oxalate and hyaluronic acid (HA) in artificial urine[86] is quantified with a tailor-made microfluidic device providing advective chaotic mixing along with monitoring the polymorphic form of the nucleating crystal as a function of time in each droplet. In a typical microfluidic induction time experiment, prescribed concentrations of aqueous $CaCl_2$ and NaOx solutions are brought in contact, as shown in Figure 1a. The two reacting solutions are dispersed in mineral oil, and the droplets of controlled size are formed in a K-junction in the "droplet formation" zone shown in Figure 1b. The content of aqueous droplets is mixed rigorously with serpentine shaped micromixers; complete advective chaotic mixing is achieved in the "mixing zone" of the device[87] (Figure 1b). The well-mixed droplets are stored and monitored in the "storage & observation zone". The nucleation and growth kinetics of two CaOx hydrates, COM and COD, under hypercalciuria and hyperoxaluria conditions using a fixed Ca and varying Ox concentration is quantified. In addition, the effect of HA on nucleation behavior has been investigated.

■ MATERIALS AND METHODS

In this section, the microfluidic device design and production, the experimental procedure for preparing the solution and monitoring crystal induction will be described.

Microfluidic Design and Device Preparation. The microfluidic device is designed to disperse a statistically significant number of well-mixed droplets acting as isolated crystallization vessels and to monitor these droplets as a function of time for nucleation kinetics measurements. The microfluidic device contains tailored micromixers and hydrodynamic traps. Three sections of the microfluidic device, namely, droplet formation, mixing, and storage & observation zones, are depicted in Figure 1b. A more detailed description of the microfluidic chip design and the optimization of the chip geometry is given in Ibis *et al.*[88] and in the S.1 section in the SI. To acquire statistically significant nucleation kinetics measurements of COM and COD under understudied conditions, both the induction time, the first moment a crystal is observed, and the pseudo-polymorphic form of the crystal are identified. The experiments are done in a thermostated room at 20 °C.

Droplet Formation and Mixing. Two aqueous artificial urine solutions and a continuous phase (oil phase) are brought together in a K shaped junction, as shown in Figure 1b for droplet generation. The droplets are stabilized by a fluorinated surfactant (Sphere Fluidics, CAS240119-1) and dispersed in the mixture of hydrofluoroether oil phase (HFE3-ethoxy-1,1,1,2,3,4,4,5,5,6,6,6-dodecafluoro-2-trifluoromethylhexane, 3 M, CAS297730−93-9). In the mixing region, serpentine-shaped bends serve as passive mixers. The serpentine passive mixers ensure complete advective chaotic mixing of droplet contents within seconds, a time scale significantly smaller than measured induction times (Figure 1b). Just after the K-junction, the serpentine shaped passive mixers are used to ensure the mixing of two aqueous streams carrying calcium and oxalate ions. While the droplets move along the serpentine passive mixers, an asymmetric drag force forms asymmetric flow patterns on droplets; consequently, the contents of droplets are mixed in each bend.[89−91]

Storage of Droplets. The droplets carrying designated concentrations of calcium, oxalate, and HA are placed in hydrodynamic traps with dimensions of 200 μm depth, 400 μm width, and 1200 μm length (in Figure 1b). The positional stability of droplets in hydrodynamic traps during the induction time measurements is critical as we want to keep track of every single droplet while capturing images. The hydrodynamic resistance of the narrow necks (180 μm) at the entrance and exit of hydrodynamic traps ensures that the trapped droplets are kept inside the traps throughout the measurement. A small change in the pressure between the reservoir and the microfluidic device will either cause the droplets to recede into the inlet tubes or proceed out of the chambers through the outlet

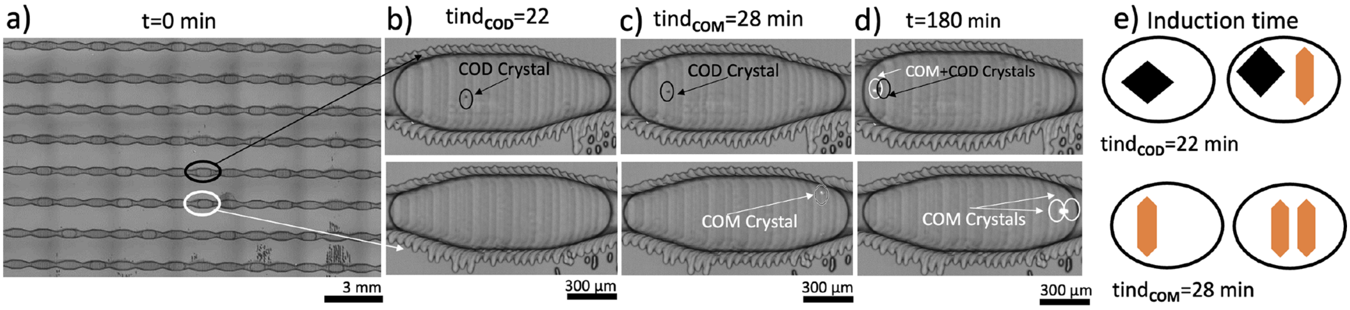

Figure 2. Polarized light microscopy images during induction time measurements with polarizer angle of 20°. (a) Observed microfluidic chip area showing droplets stored in hydrodynamic traps with 10× objective with a 20° angle, scale bar: 3 mm. Panels (b−d) show time-lapse images focusing on two droplets. In the droplet on the top panel, COD nucleates first (highlighted with a black circle) followed by nucleation of COM (highlighted with a white circle). In the second droplet, only COM crystals (highlighted with a white circle) nucleate. The images are taken with 10× objective with a 20° angle, white crystals: COM, black crystals: COD, scale bar: 300 μm. Panel (e) illustrates two populations of droplets encountered in microfluidic induction time experiments.

tube. To nullify the pressure head, we keep the reservoir and device at the same height. Furthermore, the droplets should not drift or coalesce due to the evaporation of continuous and dispersed phases through the PDMS or through ports. The proposed microfluidic chip design with built in hydrodynamic traps ensured that the trapped droplets did not drift or merge ensuring statistically significant measurements. The trapped droplets were monitored up to 5 h.

Monitoring Crystal Induction with Polarized Light Microscopy. Both the induction time and the polymorphic form of the crystals are detected with polarized light microscopy. The basic concept of crossed polarization is as follows: when a polarizer and an analyzer are oriented perpendicularly to each other, the analyzer inhibits the transmission of plane polarized light. This results in a black field of view visible via the microscope eyepiece or camera. A COD crystal is uniaxial; it has only one optical axis.[92,93] Various angles were systematically tested to determine the optimal angle allowing the identification of both COM & COD crystals. The polarized microscopy at 20° enabled identification of the COM as bright spots, while the COD appears as black spots, as shown in Figure 2. In addition to the identification of pseudo polymorphs with birefringence behavior, the crystal morphology was confirmed by high magnification imaging for a limited number of cases post-experiment. Due to the larger area of the chip and difficulties to focus on crystals inside the microfluidic chip with high magnification objectives, we could not use high magnification during the microfluidic induction time experiments. Consequently, high magnification images could only be acquired after the experiments.

Microfluidic Chip Production. The microfluidic chip is produced by a soft lithography.[43,57,88,94] The mold used in soft lithography was designed in SolidWorks, and then it is printed with a 3D printed (EnvisionTEC Micro Plus Hi-Res - 43 × 27mm). The mold was then hydrophobized to minimize the PDMS adhesion. Uncured PDMS is poured into the mold, and the PDMS is cured for 24 h as described previously by Ibis *et al.*[88] The cured PDMS is peeled from the mold to release the top PDMS section of the chip. The inlet and exit holes are prepared with a biopsy punch. The final transparent PDMS chip shown in Figure 1b is then placed on a glass slide coated with a semi-cured PDMS to ensure that the top PDMS section forms a leakage-free chip.[95]

Microfluidic Induction Time Measurements. In this section, we describe the microfluidic induction time measurements. Particularly, the procedures for image processing, induction time measurements, analysis of cumulative probability functions, and solution preparation are detailed.

Image Acquisition Procedure. When all droplets are stored in the hydrodynamic traps, the pressure pump is stopped. Immediately, an automated macro controlling the microscope stage and image acquisition is triggered. This macro ensures that the whole chip area is imaged and the acquired images are stored in a time-lapse movie. The process for the acquisition of images from the whole chip and stitching frames together takes 2 min. Once the first image is acquired, the microscope stage automatically moves to the start position and the imaging process for the second image immediately begins. Figure 2a shows a stitched image. Each image from the 5 h recorded video is manually scanned to identify the first crystal emerging in each droplet. The optical resolution of the microscope lens and camera utilized (one pixel ~0.67 μm) determines the spatial resolution for detecting a crystal in a droplet. The time point at which the first crystal is detected is regarded as the induction time of the droplet regardless whether the crystal is a COD or a COM crystal (Figure 2b,c).

Procedure for Induction Time Measurements. The droplets are imaged automatically with polarized light microscopy, in this case, a Nikon Eclipse Ti Series inverted microscope fitted with a cross polarizer and an analyzer, to observe both morphologies (COM and COD) with an optimal polarized angle chosen. 10× objective is chosen for image acquisition to get the resolution required to detect crystals while imaging the whole chip within 2 min. With this lens, half the area of the microfluidic device (middle part of the chip) could be observed. Once the middle of the chip is placed in focus, the capturing of the individual micrographs via the movement of an XY stage is started. After completing capturing of the desired area of the chip, the images are stitched together and stored constructing a time stamp image for induction time measurements. Our experimental and analytical methods allow for a clear distinction between the induction time of COD and COM. Two experiments are done for each concentration, and at least 60 droplets are collected totally (Section S.4, Table S.3 in the SI).

Analysis of Induction Time Measurements to Extract Effective Nucleation Rates of CaOx Pseudo-Polymorphs. The composite microscopy images of stored droplets at different time stamps are analyzed manually to identify the fraction of droplets with COM and COD crystals emerging as a function of time. At least 60 droplets are analyzed per experimental condition. The cumulative ratio of COM or COD crystals nucleating as a function of time is called the cumulative induction time probability function, $p(t)$. The effective nucleation rate, J, for each polymorph is calculated with a single exponential function with a delay time, an empirical function shown in eq 1.

$$p(t) = \alpha(1 - e^{-JV(t-t_g)}) = \alpha(1 - e^{-(\frac{t-t_g}{\tau})}) \qquad (1)$$

where V is the volume of the liquid phase, J is the nucleation rate, t is the time, and t_g is the delay time corresponding to the time a nucleus requires to grow to a detectable size dictated by the resolution of the microscope; the parameter τ, the average induction time, is defined as $1/JV$. While the $p(t)$ value of CaOx reaches a value of 1 when all droplets have nucleated, the $p(t)$ for COM and COD separately is the fraction of droplets in which either one of these pseudo-polymorphs nucleated first and thus forms a proportion of the $p(t)$ value of CaOx. Consequently, the $p(t)$ value of the separate hydrates does not necessarily reach the maximum value of 1. The parameter alpha (α) is a factor that accounts for the fact that two populations are observed in microfluidic induction time measurements, where $p(t)$ of COM and $p(t)$ of COD are based on the fraction of droplets in which a COM or a COD is nucleated first and represents the value of $p(t)$ at infinite time. The values for the COM and COD populations add up to a value of 1.

In microfluidic induction time measurements, the growth rate (G_{exp}) for a given experimental condition can be extracted by dividing the lower detection limit (D_{det}) of the crystals in the microscope, i.e., the size of the smallest detectable crystal, by the t_g value; $G_{exp} = D_{det}/t_g$. To calculate G_{exp}, D_{det} is estimated as 4 pixels (1 pixel ≈ 0.67 micrometers) corresponding to 2.7 micrometers based on the resolution of the microscope images used to detect the crystals. It should be noted that these growth rates are averaged over all crystals contributing.

Preparation of Artificial Urine. In our work, the composition of artificial urine selected is based on Streit *et al.*,[86] shown in Table 1, with adjustments to calcium and oxalate levels and HA additive when necessary.

Table 1. Ingredients of Artificial Urine (The Measured pH Value of Artificial Urine Is 5.57)

compounds	molarity [mM]	source
sodium chloride (NaCl)	90	Fluka
potassium chloride (KCl)	42	Emsure
ammonium chloride (NH_4Cl)	20	Sigma-Aldrich
creatinine ($C_4H_7N_3O$)	7	Sigma-Aldrich
urea (CH_4N_2O)	300	Emprove
tri sodium citrate ($Na_3C_6H_5O_7$)	2	Emprove
magnesium sulfate heptahydrate ($MgSO_4\cdot 7H_2O$)	2	Sigma-Aldrich
sodium sulfate ($NaSO_4$)	13	Sigma-Aldrich
sodium phosphate monobasic (NaH_2PO_4)	16	Sigma-Aldrich

To prepare artificial urine, each chemical (see Table 1) is weighed and dissolved in ultrapure water (ELGA PURELAB, Resistivity:18.2 MΩ·cm at 23.6 °C). The glassware used and microfluidic chip are rigorously rinsed with ultrapure water to minimize contamination. To accurately control the concentration of calcium and oxalate in the droplets, designated calcium and oxalate concentrations are reached by dissolving known amounts of either $CaCl_2$ or NaOx in separate artificial urine solutions. The prepared solutions are rigorously mixed using an ultrasonicator (Branson 2510, Ultrasonic Cleaner) for 20 min at 20°C. After dissolution, both solutions carrying calcium and oxalate ions are filtered (Whatman, 0.45 μm pore diameter filters). Mixing calcium and oxalate solutions, droplet formation and filling the entire channel with droplets is completed in 10 s. The moment image acquisition starts right after the channel is filled is registered as $t = 0$. As the time required for droplet formation, mixing, and filling operations take significantly less time than the image acquisition of 2 min, the major experimental uncertainty comes from image acquisition. Any induction time below 2 min cannot be accurately measured with the proposed setup.

Solution Preparation for Microfluidic Experiments. Calcium chloride ($CaCl_2$) and sodium oxalate (NaOx) are dissolved in 50 mL of basis artificial urine (AU) separately into two beakers. These two solutions are connected to two different microfluidic device inlets. When the pressure pump is started, solutions move from the inlet and merge into a droplet. Once the streams merge, the concentration of $CaCl_2$ and NaOx solutions fed to inlets are diluted by a factor of two, reaching the desired concentrations inside the droplets. The final concentration of $CaCl_2$ is 6.0 mM, and those of NaOx are 0.5, 0.85, and 1.2 mM in the droplets.

For inhibition experiments with HA, the droplets contain the concentrations as 6 mM of $CaCl_2$ and 0.85 mM of NaOx with three different HA solutions: 0.035, 0.25, 0.50 mg/mL in artificial urine. HA is dissolved in an aqueous stream containing NaOx and sent to the device just from one inlet to protect the reaction with the calcium ion. To avoid contamination, all solutions for microfluidic induction time experiments are made fresh for each experiment.

■ RESULTS AND DISCUSSION

Microfluidic nucleation induction time measurements were used to quantify the effect of varying levels of added oxalate and HA on the kinetics of CaOx nucleation from solution. The ability to determine both the time and the type of pseudo-polymorphic form of the nucleating crystals resulted in interesting observations. In all experiments, two distinct droplet populations, as shown and illustrated in Figure 2d,e were found that were representative for all our observations. In the droplet population illustrated in the top panel of Figure 2e, COD crystals nucleated first followed by COM crystal nucleation at later times. In a second population illustrated in the bottom panel of Figure 2e, a COM crystal nucleated first, and only COM crystals nucleated at later time points.

Initially, we focus on the effect of increasing oxalate concentration at fixed calcium concentration in the artificial urine in Figure 3. Figure 3a gives the nucleation probability distribution function of all CaOx crystals irrespective of the crystal hydrate form (either COD or COM). As expected, the $p(t)$ curves observed in Figure 3a reach unity faster at higher oxalate concentrations. This behavior can be attributed to increased supersaturation in the samples with the higher

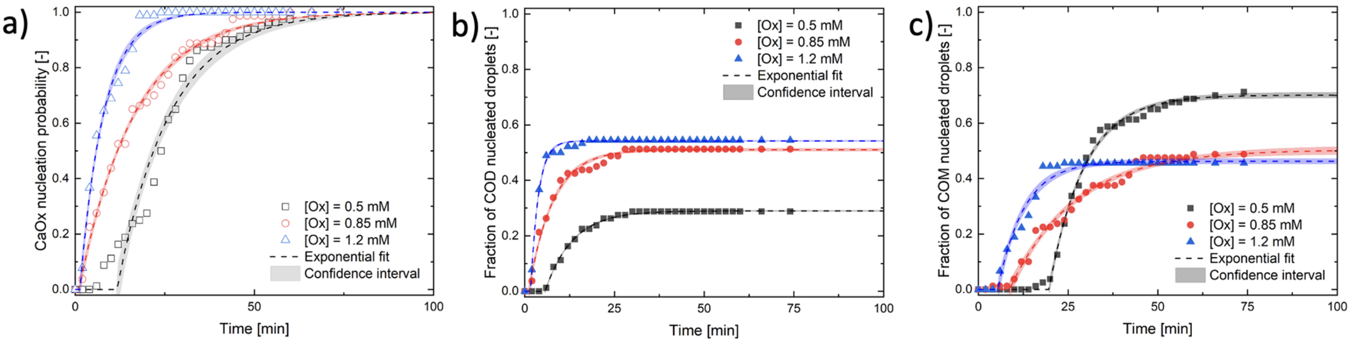

Figure 3. Cumulative induction time probability curves, $p(t)$ for (a) COD and COM, (b) only COD crystals, and (c) only COM crystals where the $C_2O_4^{2-}$ concentrations, [Ox] is varied at a fixed Ca^{2+} concentration of 6.0 mM in artificial urine. The $p(t)$ curves are fitted with the exponential function with delay time (eq 1).

Table 2. The Fitted Parameters, Standard Errors, and the Error Statistics of the Fits from a Single Exponential Model with a Delay Time of COD and COM for the Different Added Oxalate Concentrations (MSE Stands for Mean Squared Error)

single exponential model for COD and COM with additive different amounts of oxalate											
		alpha		detection time		nucleation rate		delay time		growth rate	
		(α)		(τ) [min]		(J) [m^{-3} min^{-1}]		(tg) [min]		[m/s]	statistics
	[10^{-3} M] Ox	value	std error	value	std error	value	std error	value	std error	G_{exp}	MSE
COD	0.5	0.290	1×10^{-3}	7.6	0.2	2.66×10^{10}	7×10^{8}	5.7	0.1	7×10^{-9}	5×10^{-3}
	0.85	0.510	3×10^{-3}	6.7	0.3	3.02×10^{10}	8×10^{8}	1.1	0.2	4×10^{-8}	1×10^{-2}
	1.2	0.542	1×10^{-3}	2.1	0.1	9.6×10^{10}	3×10^{9}	1.7	0.0	2×10^{-8}	8×10^{-3}
COM	0.5	0.701	5×10^{-3}	9.9	0.4	2.05×10^{10}	6×10^{8}	19.7	0.2	2×10^{-9}	2×10^{-2}
	0.85	0.504	8×10^{-3}	18.2	1.2	1.11×10^{10}	3×10^{8}	8.7	0.6	5×10^{-9}	2×10^{-2}
	1.2	0.462	5×10^{-3}	7.3	0.6	2.77×10^{10}	8×10^{8}	5.4	0.4	8×10^{-9}	2×10^{-2}

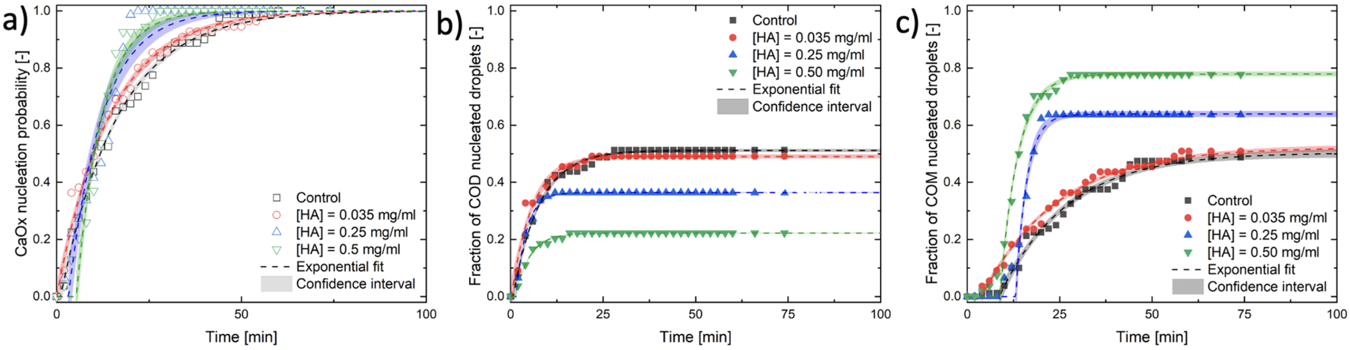

Figure 4. Cumulative induction time probability curves, $p(t)$, for (a) COD and COM, (b) only COD crystals, and (c) only COM crystals where HA concentrations are varied at fixed Ca^{2+} and $C_2O_4^{2-}$ concentrations in artificial urine fitted with the exponential function with delay time (eq 1). Added molar concentrations of HA are 0.035, 0.25, and 0.50 mg/mL at fixed Ca^{2+}; 6.0 mM and $C_2O_4^{2-}$; 0.85 mM in artificial urine.

oxalate concentrations. Using polarized light microscopy, we were able to quantify the nucleation kinetics of COM and COD independently. Figure 3b reports the ratio of droplets in which COD nucleated first, while Figure 3c shows the ratio of droplets in which a COM crystal was first observed as a function of time.

The fraction of the droplets in which COD nucleated first seems to be proportional to the added oxalate concentration (or the supersaturation), as shown in Figure 3b. On the other hand, in the second population where a COM crystal nucleated first, no COD but only COM crystals were observed at later time points. Moreover, the ratio of the droplets in which COM nucleated first was inversely proportional to the added oxalate concentration (and thus the supersaturation) as shown in Figure 3c. In addition, the $p(t)$ curves of COM display lower slopes and larger delay times compared to the $p(t)$ curves of COD nucleation.

The nucleation probability curves for CaOx, irrespective of the type of hydrate, as well as for the probability distribution of droplets in which COD or COM nucleation occurred first were fitted with an exponential function with delay time (eq 1), as shown in Figure 3. The fitting procedure provided estimates of delay time (t_g), induction time (τ), and nucleation rate (J), as well as the proportion of each pseudo-polymorph formed (α), given in Table 2. The fits are also shown in Figure 3 as dashed curves, with the confidence intervals of the fits shown as the shaded area around the fits.

Comparison of the fit parameters for COD and COM for all the oxalate concentrations studied reveals that the induction times for COD are always shorter than those for COM nucleation, which means that the nucleation rate of COD is higher than that of COM under identical conditions. Looking at the α values in Table 2, i.e., the values at which the fraction of droplets saturate in Figure 3b,c, we can also conclude that at high oxalate concentrations, the formation of the metastable form COD is favored over the stable form COM. At lower oxalate concentrations COM nucleation appears to be dominant (the alpha value for COM increases from 0.46 to 0.70 with decreasing oxalate concentrations), see Figure 3c and Table 2.

Daudon *et al.*[96] observed that once the Ca:Ox molar ratio is between 5 and 14, a mixture of COM and COD crystals is present in urine. It is noteworthy to mention that the frequency of finding COM is much higher than that of COD in the patient's kidney stones.[4] Interpretation of this medical observation in the context of our results would indicate that nucleation of CaOx in most patients may be occurring at a lower Ca:Ox ratio, a condition where COM nucleates faster than COD, despite the fact that the frequency of droplets in which COD nucleated first was slightly higher. It is important to highlight that every droplet where COD was detected first also showed COM nucleation after some time. Yet, this interpretation operates under the assumption that the artificial urine used in this study is a very good representative of patient urine. In reality, the patient urine contains more complex macromolecules and dead cells, and its composition varies constantly in response to environmental changes. It is noteworthy that a solution-mediated transformation from COD to COM could also explain the dominant COM content in kidney stones. In our experiments, a transformation from COD into COM was not detected in the droplets, possibly due to limitations on experiment duration, the inability to observe the crystal structure at the nanoscale, or the molar ratios of Ca:Ox used.[97]

Table 3. The Fitted Parameters with 95% Confidence Intervals and the Corresponding Statistics from the Single Exponential Model with Delay Time for the Different Amount HA Conditions (MSE Stands for Mean Squared Error)

single exponential model of COD and COM for the different amount HA conditions											
		alpha		detection time		nucleation rate		delay time		growth rate	
		(α)		(τ) [min]		(J) [m^{-3} min^{-1}]		(t_g) [min]		[m/s]	statistics
	mg/ml HA	value	std error	value	std error	value	std error	value	std error	G_{exp}	MSE
COD	control	0.510	2×10^{-3}	6.7	0.3	3.02×10^{10}	8×10^{8}	1.1	0.2	4×10^{-8}	1×10^{-2}
	0.035	0.490	3×10^{-3}	5.5	0.5	3.7×10^{10}	1×10^{9}	0.2	0.4	2×10^{-7}	2×10^{-2}
	0.25	0.3643	7×10^{-4}	2.9	0.1	7.1×10^{10}	2×10^{9}	1.44	0.05	3×10^{-8}	4×10^{-3}
	0.50	0.2221	6×10^{-4}	3.9	0.1	5.1×10^{10}	1×10^{9}	1.2	0.1	3×10^{-8}	4×10^{-3}
COM	control	0.504	8×10^{-3}	18.1	1.2	1.11×10^{10}	3×10^{8}	8.7	0.6	8×10^{-8}	2×10^{-2}
	0.035	0.523	5×10^{-3}	20.4	0.8	9.91×10^{9}	3×10^{8}	3.9	0.4	1×10^{-7}	1×10^{-2}
	0.25	0.639	5×10^{-3}	3.0	0.3	6.85×10^{10}	2×10^{9}	13.1	0.2	2×10^{-7}	2×10^{-2}
	0.50	0.779	4×10^{-3}	4.8	0.3	4.22×10^{10}	1×10^{9}	8.9	0.2	2×10^{-7}	2×10^{-2}

Table 2 also shows that the values for the t_g decrease with the increase in the oxalate concentration for both of COD and COM crystals indicating an increase in the growth rate.

For all oxalate concentrations, the delay time, t_g, for COD is shorter than for COM indicating that the COD grows faster to a detectable size (see Analysis of Induction Time Measurements to Extract Effective Nucleation Rates of CaOx Pseudo-Polymorphs). Interestingly, increasing the oxalate concentration has a stronger effect on the growth rate of COM than of COD crystals.

An increasing oxalate concentration from 0.5×10^{-3} to 1.2×10^{-3} M caused a decrease in the molar ratio of Ca:Ox and increased the COD nucleation rate. Remarkably, the COD nucleation rate increases more than a factor of three from 2.66×10^{10} to 9.57×10^{10} m^{-3} min^{-1}, whereas for COM, the nucleation rates only slightly increase from 2.05×10^{10} to 2.55×10^{10} m^{-3} min^{-1} (see Table 2).

Figure 4a shows the effect of the addition of different concentrations of HA on the $p(t)$ curves of CaOx irrespective of the crystal hydrate form. The fraction of the droplets of where COD and COM nucleated first are given in Figure 4b,c, respectively. The dashed lines are fits to eq 1 with 95% confidence intervals shown as shaded regions. The numerical values of the determined α, τ, J, and t_g values are given in Table 3 together with the confidence intervals and the statistical errors of the estimated values.

At first glance, the $p(t)$ curves in Figure 4a do not reveal a pronounced trend. Both the $p(t)$ curves for an HA concentration of 0.035 mg/mL and the control as well as the curves for HA concentrations of 0.25 and 0.5 mg/mL appear to overlap. Increasing the concentration of HA at fixed calcium and oxalate concentrations appears to slightly increase CaOx nucleation kinetics, yet the effect of HA on nucleation kinetics appears to be small. A different picture emerges when the fraction of droplets where COD and COM nucleated first are plotted. The fraction of the droplets in which COD nucleated first decreases with increasing HA concentrations evident from the values for COD in Table 3 and the plateaus observed at later times (>50 min) in Figure 4b. Furthermore, Figure 4c shows the opposite trend for the droplets in which a COM crystal nucleated first. The fraction of the droplets nucleated as COM increased (α increased from 0.50 to 0.78) with increasing HA concentrations. This followed the trend also observed for the nucleation rate for COM, which increased under the same conditions (see Table 3). In contrast, the droplets where COD nucleated first showed only a marginal increase in the nucleation rate.

Looking at the results of the control experiment (without HA) and those of 0.035 mg/mL HA, the delay times for COD decrease from 1.09 to 0.22 and for COM from 8.65 to 3.88. The lowest HA concentration, 0.035 mg/mL HA, does not show any effect on nucleation rates and alpha values for any of the pseudo-polymorphs, while the growth rate visibly increases in both cases. The highest nucleation rate of COD, 7.10×10^{10} m^{-3} min^{-1} and the highest nucleation rate of COM, 6.85×10^{10} m^{-3} min^{-1} are observed at 0.25 mg/mL HA.

Delay times increase for COD from 0.22 to 1.44 and for COM from 3.88 to 13.12 (compared to 0.035 mg/mL HA). Surprisingly the increment from 0.25×10^{-3} to 0.5 mg/mL HA decreases the nucleation rate for both COD and COM, i.e., from 7.1×10^{10} to 5.1×10^{10} m^{-3} min^{-1} and from 6.8×10^{10} to 4.2×10^{10} m^{-3} min^{-1}, respectively, while the delay time decreases, implying an increase in the growth rate when increasing the HA concentration from 0.25 to 0.5 mg/mL (see Table 3).

At this point, it is informative to compare our results with liter scale experiments presented by Polat and Eral despite significantly different scales and protocols involved.[42] Polat and Eral characterized CaOx crystals forming a post-reaction with methods such as scanning electron microscopy, atomic force microscopy, and thermogravimetric analysis.[42] In this bulk crystallization study conducted in a well-stirred, liter size vessel at a Ca:Ox ratio of 20, COD crystals were sparsely observed with increasing HA concentration in water where the control experiments conducted without HA produced only COM. Identical experiments conducted in artificial urine produced only COD with and without HA. In other words, all crystals nucleated as COD both in control and in the presence of HA in artificial urine. At a first sight, one may think that results of Polat and Eral[42] contradict reported results in this study. A closer inspection reveals that the bulk experiments of Polat and Eral[42] were conducted at a significantly higher Ca:Ox ratio with rigorous mixing at 37 °C using slightly different procedures. We suspect that the combined effect of the high Ca:Ox ratio in experiments of Polat and Eral[42] and mixing might collectively induce a higher rate of COD nucleation in the liter size vessel overshadowing the potential emergence of COM in all artificial urine samples due to the presence of HA. Mixing triggered secondary nucleation influencing resulting inthe polymorphic form has been previously reported in L-glutamic acid.[98] Moreover, our control experiments conducted at a Ca:Ox ratio of 7 produced almost a 50/50 mixture of COM and COD; hence, the change in COM & COD nucleation rates upon the addition of HA can be easily detected unlike the experiments of Polat and Eral[42] where the control experiment produced 100% COD. In addition, our experimental procedure focuses on the first crystal nucleating in the droplet while Polat and Eral[42] reported collected crystals after precipitation. Another significant difference is the larger surface area to volume ratio in microfluidic droplets compared to bulk experiments. The larger surface per volume ratio might enhance the heterogeneous nucleation rate of COM in the presence of HA in our study. Surfactants at air−liquid interfaces have been previously reported to influence phase transitions.[61] This comparison points out that the rate of COM and COD nucleation as well as their transition may be influenced by stirring and the presence of interfaces, hence opening new alleys of investigation while emphasizing the relevance of our study at a length scale comparable to collecting duct.

In the medical literature, HA is recognized to play a role in cell adherence prevention, in other words, the blockage of crystal binding to epithelial cells.[4] Interestingly, it is hypothesized that the epithelial cell membranes express HA to prevent kidney stone formation yet HA is also overexpressed if epithelial cells are damaged due to hydrodynamic stress or impact of stone fragments.[4] HA has been studied in the context of cell−stone interactions, yet how HA influences nucleation and growth kinetics remains underexplored.

Lamontagne *et al.* worked on the interaction of HA and the CaOx stone by focusing on the adhesion of the HA.[36] These authors reported that HA binds at the [100] face of COM crystals. They found that saturated calcium oxalate condition leads to interactions between the HA and COM.[36] Daudon *et al.* observed that COM crystals were predominant in urine once the molar ratio of Ca:Ox was less than 5.[96,97] These reports in the literature may help rationalizing the trend shown in Figure 4 where increasing HA concentration results in a higher fraction of the COM droplets. As HA binds to COM crystals[36] and COM crystals are predominantly observed for a molar ratio of Ca:Ox less than 5,[96] it can be expected that increasing HA concentration may result in a smaller molar ratio of Ca:Ox. Because COM crystals are closely connected with kidney stone illness, the discovery of additive-mediated suppression of COM but preferred COD production is noteworthy.[99−101] Since COD is less frequently linked to epithelial cells at the tip of the renal papilla than COM, it is, consequently, easier to remove from the organ with the urine.[99] Therefore, by controlling the pseudo-polymorph of CaOx stone with an additive like HA, favoring COM upon COD might be helpful for the medical treatment in preventing the adhesion to cells and further growth of renal calculi.

■ CONCLUSIONS

We present the nucleation kinetics of CaOx at varying concentrations of oxalate and HA in artificial urine using droplet microfluidics technology. The unique contribution of this work is the ability to extract the kinetics of individual CaOx hydrates as COD and COM instead of considering them as a CaOx crystal. An increase in the oxalate concentration increases the fraction of COD nucleation and slows down the growth of COD crystals in artificial urine. We observed that in droplets where COD nucleated, COM crystals emerged at later times. However, when COM nucleated first, COD was not formed within the experimental time scale. An antagonistic effect of HA on the fraction of COD and COM was observed. HA promoted COM formation while inhibiting COD. Moreover, it is observed that the COD nucleation rate is always higher than the COM nucleation rate for each experimental condition studied. This study highlights the underlying mechanism of the effect of HA on CaOx stone formation. The results can be helpful for the medical treatment by bringing understanding of COD over COM using HA as an additive.

■ ASSOCIATED CONTENT

Supporting Information

The Supporting Information is available free of charge at https://pubs.acs.org/doi/10.1021/acs.cgd.2c00198.

Microfluidic device, droplet image at end of the experiment, and extended tables for single exponential model of COD and COM (PDF)

■ AUTHOR INFORMATION

Corresponding Author

Huseyin Burak Eral − *Complex Fluid Processing, Process & Energy Department, Delft University of Technology, 2628 CB Delft, The Netherlands; Van't Hoff Laboratory for Physical and Colloid Chemistry, Debye Institute for Nanomaterials Science Utrecht University, 3584 CH Utrecht, The Netherlands;* orcid.org/0000-0003-3193-452X; Email: H.B.Eral@tudelft.nl

Authors

Fatma Ibis − *Complex Fluid Processing, Process & Energy Department, Delft University of Technology, 2628 CB Delft, The Netherlands;* orcid.org/0000-0001-6230-0269

Manzoor Alhaji Nuhu − *Complex Fluid Processing, Process & Energy Department, Delft University of Technology, 2628 CB Delft, The Netherlands*

Frederico Marques Penha − *Department of Chemical Engineering, KTH Royal Institute of Technology, SE100-44 Stockholm, Sweden;* orcid.org/0000-0001-7614-8448

Tsun Wang Yu − *Complex Fluid Processing, Process & Energy Department, Delft University of Technology, 2628 CB Delft, The Netherlands*

Antoine E. D. M. van der Heijden − *Complex Fluid Processing, Process & Energy Department, Delft University of Technology, 2628 CB Delft, The Netherlands*

Herman J. M. Kramer − *Complex Fluid Processing, Process & Energy Department, Delft University of Technology, 2628 CB Delft, The Netherlands;* orcid.org/0000-0003-3580-8432

Complete contact information is available at: https://pubs.acs.org/10.1021/acs.cgd.2c00198

Author Contributions

The manuscript was written through the contributions of all authors. All authors have given approval to the final version of the manuscript.

Notes

The authors declare no competing financial interest.

■ ACKNOWLEDGMENTS

Authors would like to thank Prof.dr. Chris Bangma, Prof.dr. Ir. Wytske M. van Weerden, and Prof.dr. Guido Jenster for fruitful discussions and Wilma J. Teubel for her valuable help in cell

culture experiments in the Department of Urology, Erasmus University Medical Center, Erasmus MC Cancer Institute, Rotterdam, The Netherlands.

■ REFERENCES

(1) Khan, S. R.; Pearle, M. S.; Robertson, W. G.; Gambaro, G.; Canales, B. K.; Doizi, S.; Traxer, O.; Tiselius, H.-G. Kidney stones. *Nat. Rev. Dis. Primers* **2016**, *2*, 1−23.

(2) Bushinsky, D. A.; Asplin, J. R.; Grynpas, M. D.; Evan, A. P.; Parker, W. R.; Alexander, K. M.; Coe, F. L. Calcium oxalate stone formation in genetic hypercalciuric stone-forming rats. *Kidney Int.* **2002**, *61*, 975−987.

(3) Uribarri, J.; Oh, M. S.; Carroll, H. J. The first kidney stone. *Ann. Intern. Med.* **1989**, *111*, 1006−1009.

(4) Alelign, T.; Petros, B. Kidney stone disease: an update on current concepts. *Adv. Urol.* **2018**, *2018*, 1.

(5) Ridley, J. W., *Fundamentals of the Study of Urine and Body Fluids*. Springer: 2018, DOI: 10.1007/978-3-319-78417-5.

(6) Bono, M. J.; Reygaert, W. C. Urinary tract infection. In *StatPearls [Internet]*; StatPearls Publishing, 2018.

(7) Worcester, E. M.; Coe, F. L. Nephrolithiasis. *Primary Care: Clin. Off. Pract.* **2008**, *35*, 369−391.

(8) Scales, C. D., Jr.; Smith, A. C.; Hanley, J. M.; Saigal, C. S.; Urologic Diseases in America Project. Prevalence of kidney stones in the United States. *Eur. Urol.* **2012**, *62*, 160−165.

(9) Long, L. O.; Park, S. Update on nephrolithiasis management. *Minerva Nefrol.=Ital. J. Urol. Nephrol.* **2007**, *59*, 317−325.

(10) Rule, A. D.; Lieske, J. C.; Li, X.; Melton, L. J., III; Krambeck, A. E.; Bergstralh, E. J. The ROKS nomogram for predicting a second symptomatic stone episode. *J. Am. Soc. Nephrol.* **2014**, *25*, 2878−2886.

(11) Evan, A. P. Physiopathology and etiology of stone formation in the kidney and the urinary tract. *Pediatr. Nephrol.* **2010**, *25*, 831−841.

(12) Takazawa, R.; Kitayama, S.; Tsujii, T. Appropriate kidney stone size for ureteroscopic lithotripsy: When to switch to a percutaneous approach. *World J. Nephrol.* **2015**, *4*, 111.

(13) Finlayson, B. Physicochemical aspects of urolithiasis. *Kidney Int.* **1978**, *13*, 344−360.

(14) Grases, F.; Villacampa, A. I.; Söhnel, O.; Königsberger, E.; May, P. M. Phosphate Composition of Precipitates from Urine-like Liquors. *Cryst. Res. Technol.* **1997**, *32*, 707−715.

(15) Ratkalkar, V. N.; Kleinman, J. G. Mechanisms of stone formation. *Clin. Rev. Bone Miner. Metab.* **2011**, *9*, 187−197.

(16) Moe, O. W. Kidney stones: pathophysiology and medical management. *Lancet* **2006**, *367*, 333−344.

(17) Hanno, P. M.; Guzzo, T. J.; Malkowicz, S. B.; Wein, A. J. *Penn clinical manual of urology*; Elsevier Health Sciences, 2007.

(18) Ogawa, Y.; Miyazato, T.; Hatano, T. Oxalate and urinary stones. *World J. Surg.* **2000**, *24*, 1154−1159.

(19) Robertson, W. G.; Peacock, M. The cause of idiopathic calcium stone disease: hypercalciuria or hyperoxaluria? *Nephron* **1980**, *26*, 105−110.

(20) Bhasin, B.; Ürekli, H. M.; Atta, M. G. Primary and secondary hyperoxaluria: Understanding the enigma. *World J. Nephrol.* **2015**, *4*, 235.

(21) Parks, J. H.; Coward, M.; Coe, F. L. Correspondence between stone composition and urine supersaturation in nephrolithiasis. *Kidney Int.* **1997**, *51*, 894−900.

(22) Weber, D. V.; Coe, F. L.; Parks, J. H.; Dunn, M. S. L.; Tembe, V. Urinary saturation measurements in calcium nephrolithiasis. *Ann. Intern. Med.* **1979**, *90*, 180−184.

(23) Kok, D. J.; Papapoulos, S. E. Physicochemical considerations in the development and prevention of calcium oxalate urolithiasis. *Bone Miner.* **1993**, *20*, 1−15.

(24) Favus, M. J.; Zeytinoglu, M.; Coe, F. L., Idiopathic hypercalciuria and nephrolithiasis. In *Vitamin D*; Elsevier, 2018; pp. 485−505.

(25) Asplin, J. R. Hyperoxaluric calcium nephrolithiasis. *Endocrinol. Metab. Clin.* **2002**, *31*, 927−949.

(26) Milliner, D. S. The primary hyperoxalurias: an algorithm for diagnosis. *Am. J. Nephrol.* **2005**, *25*, 154−160.

(27) Robijn, S.; Hoppe, B.; Vervaet, B. A.; D'haese, P. C.; Verhulst, A. Hyperoxaluria: a gut−kidney axis? *Kidney Int.* **2011**, *80*, 1146−1158.

(28) Basavaraj, D. R.; Biyani, C. S.; Browning, A. J.; Cartledge, J. J. The role of urinary kidney stone inhibitors and promoters in the pathogenesis of calcium containing renal stones. *EAU-EBU Update Ser.* **2007**, *5*, 126−136.

(29) Aggarwal, K. P.; Narula, S.; Kakkar, M.; Tandon, C. Nephrolithiasis: molecular mechanism of renal stone formation and the critical role played by modulators. *BioMed Res. Int.* **2013**, *2013*, 1.

(30) Verhulst, A.; Asselman, M.; Persy, V. P.; Schepers, M. S. J.; Helbert, M. F.; Verkoelen, C. F.; De Broe, M. E. Crystal retention capacity of cells in the human nephron: involvement of CD44 and its ligands hyaluronic acid and osteopontin in the transition of a crystal binding-into a nonadherent epithelium. *J. Am. Soc. Nephrol.* **2003**, *14*, 107−115.

(31) Horkay, F.; Basser, P. J.; Londono, D. J.; Hecht, A.-M.; Geissler, E. Ions in hyaluronic acid solutions. *J. Chem. Phys.* **2009**, *131*, 184902.

(32) Verkoelen, C. F. Crystal retention in renal stone disease: a crucial role for the glycosaminoglycan hyaluronan? *J. Am. Soc. Nephrol.* **2006**, *17*, 1673−1687.

(33) Borges, F. T.; Michelacci, Y. M.; Aguiar, J. A. K.; Dalboni, M. A.; Garófalo, A. S.; Schor, N. Characterization of glycosaminoglycans in tubular epithelial cells: calcium oxalate and oxalate ions effects. *Kidney Int.* **2005**, *68*, 1630−1642.

(34) Gan, Q.-Z.; Sun, X.-Y.; Bhadja, P.; Yao, X.-Q.; Ouyang, J.-M. Reinjury risk of nano-calcium oxalate monohydrate and calcium oxalate dihydrate crystals on injured renal epithelial cells: aggravation of crystal adhesion and aggregation. *Int. J. Nanomed.* **2016**, *11*, 2839.

(35) Asselman, M.; Verhulst, A.; De Broe, M. E.; Verkoelen, C. F. Calcium oxalate crystal adherence to hyaluronan-, osteopontin-, and CD44-expressing injured/regenerating tubular epithelial cells in rat kidneys. *J. Am. Soc. Nephrol.* **2003**, *14*, 3155−3166.

(36) Lamontagne, C. A.; Plante, G. E.; Grandbois, M. Characterization of hyaluronic acid interaction with calcium oxalate crystals: implication of crystals faces, pH and citrate. *J. Mol. Recognit.* **2011**, *24*, 733−740.

(37) Verkoelen, C. F.; van Der Boom, B. G.; Romijn, J. C. Identification of hyaluronan as a crystal-binding molecule at the surface of migrating and proliferating MDCK cells. *Kidney Int.* **2000**, *58*, 1045−1054.

(38) Xie, B.; Halter, T. J.; Borah, B. M.; Nancollas, G. H. Aggregation of calcium phosphate and oxalate phases in the formation of renal stones. *Cryst. Growth Des.* **2015**, *15*, 204−211.

(39) Gardner, G. L.; Nancollas, G. H. Kinetics of dissolution of calcium oxalate monohydrate. *J. Phys. Chem.* **1975**, *79*, 2597−2600.

(40) Hsu, Y.-C.; Lin, Y.-H.; Shiau, L.-D. Effects of various inhibitors on the nucleation of calcium oxalate in synthetic urine. *Crystals* **2020**, *10*, 333.

(41) Cerini, C.; Geider, S.; Dussol, B.; Hennequin, C.; Daudon, M.; Veesler, S.; Nitsche, S.; Boistelle, R.; Berthézène, P.; Dupuy, P.; Vazi, A.; Berland, Y.; Dagorn, J. C.; Verdier, J. M. Nucleation of calcium oxalate crystals by albumin: involvement in the prevention of stone formation. *Kidney Int.* **1999**, *55*, 1776−1786.

(42) Polat, S.; Eral, H. B. Elucidating the role of hyaluronic acid in the structure and morphology of calcium oxalate crystals. *Adv. Powder Technol.* **2021**, *32*, 3650−3659.

(43) Pleeging, R. M. B.; Ibis, F.; Fan, D.; Sasso, L.; Eral, H. B.; Staufer, U. Polymer nano manufacturing of a biomimicking surface for kidney stone crystallization studies. *Micro Nano Eng.* **2021**, *13*, 100094.

(44) Schuurmans, C. C. L.; Abbadessa, A.; Bengtson, M. A.; Pletikapic, G.; Eral, H. B.; Koenderink, G.; Masereeuw, R.; Hennink, W. E.; Vermonden, T. Complex coacervation-based loading and

tunable release of a cationic protein from monodisperse glycosaminoglycan microgels. *Soft Matter* **2018**, *14*, 6327−6341.

(45) Akbarieh, M.; Tawashi, R. Calcium oxalate crystal growth in the presence of mucin. *Scanning Microsc.* **1991**, *5*, 12.

(46) Farmanesh, S.; Ramamoorthy, S.; Chung, J.; Asplin, J. R.; Karande, P.; Rimer, J. D. Specificity of growth inhibitors and their cooperative effects in calcium oxalate monohydrate crystallization. *J. Am. Chem. Soc.* **2014**, *136*, 367−376.

(47) Laffite, G.; Leroy, C.; Bonhomme, C.; Bonhomme-Coury, L.; Letavernier, E.; Daudon, M.; Frochot, V.; Haymann, J.-P.; Rouzière, S.; Lucas, I. T.; Bazin, D.; Babonneau, F.; Abou-Hassan, A. Calcium oxalate precipitation by diffusion using laminar microfluidics: toward a biomimetic model of pathological microcalcifications. *Lab Chip* **2016**, *16*, 1157−1160.

(48) Gombedza, F.; Evans, S.; Shin, S.; Boadi, E. A.; Zhang, Q.; Nie, Z.; Bandyopadhyay, B. C. Melamine promotes calcium crystal formation in three-dimensional microfluidic device. *Sci. Rep.* **2019**, *9*, 1−14.

(49) Laval, P.; Salmon, J.-B.; Joanicot, M. A microfluidic device for investigating crystal nucleation kinetics. *J. Cryst. Growth* **2007**, *303*, 622−628.

(50) Zheng, B.; Roach, L. S.; Ismagilov, R. F. Screening of protein crystallization conditions on a microfluidic chip using nanoliter-size droplets. *J. Am. Chem. Soc.* **2003**, *125*, 11170−11171.

(51) Nisisako, T.; Torii, T.; Higuchi, T. Droplet formation in a microchannel network. *Lab Chip* **2002**, *2*, 24−26.

(52) *3D Printer*; https://envisiontec.com/3d-printers/desktop-3d-printers/micro-plus-hi-res/.

(53) Ai, Y.; Xie, R.; Xiong, J.; Liang, Q. Microfluidics for Biosynthesizing: from Droplets and Vesicles to Artificial Cells. *Small* **2020**, 1903940.

(54) Tona, R. M.; McDonald, T. A. O.; Akhavein, N.; Larkin, J. D.; Lai, D. Microfluidic Droplet Liquid Reactors for Active Pharmaceutical Ingredient Crystallization by Diffusion Controlled Solvent Extraction. *Lab Chip* **2019**, 2127.

(55) Li, S.; Ihli, J.; Marchant, W. J.; Zeng, M.; Chen, L.; Wehbe, K.; Cinque, G.; Cespedes, O.; Kapur, N.; Meldrum, F. C. Synchrotron FTIR mapping of mineralization in a microfluidic device. *Lab Chip* **2017**, *17*, 1616−1624.

(56) Sia, S. K.; Whitesides, G. M. Microfluidic devices fabricated in poly (dimethylsiloxane) for biological studies. *Electrophoresis* **2003**, *24*, 3563−3576.

(57) An, H. Z.; Eral, H. B.; Chen, L.; Chen, M. B.; Doyle, P. S. Synthesis of colloidal microgels using oxygen-controlled flow lithography. *Soft Matter* **2014**, *10*, 7595−7605.

(58) Gupta, A.; Badruddoza, A. Z. M.; Doyle, P. S. A general route for nanoemulsion synthesis using low-energy methods at constant temperature. *Langmuir* **2017**, *33*, 7118−7123.

(59) Baroud, C. N.; Gallaire, F.; Dangla, R. Dynamics of microfluidic droplets. *Lab Chip* **2010**, *10*, 2032−2045.

(60) Irimia, D.; Jose Shirley, J.; Garg, A. S.; Nijland, D. P. A.; van der Heijden, A. E. D. M.; Kramer, H. J. M.; Eral, H. B. Influence of Laser Parameters and Experimental Conditions on Nonphotochemical Laser-Induced Nucleation of Glycine Polymorphs. *Cryst. Growth Des.* **2021**, 631.

(61) Penha, F. M.; Gopalan, A.; Meijlink, J. C.; Ibis, F.; Eral, H. B. Selective Crystallization of d-Mannitol Polymorphs Using Surfactant Self-Assembly. *Cryst. Growth Des.* **2021**, 3928.

(62) Fleisch, H. Inhibitors and promoters of stone formation. *Kidney Int.* **1978**, *13*, 361−371.

(63) Downey, J. A.; Nickel, J. C.; Clapham, L.; McLean, R. J. C. In vitro inhibition of struvite crystal growth by acetohydroxamic acid. *Br. J. Urol.* **1992**, *70*, 355−359.

(64) Jones, D. S.; Djokic, J.; Gorman, S. P. Characterization and optimization of experimental variables within a reproducible bladder encrustation model and in vitro evaluation of the efficacy of urease inhibitors for the prevention of medical device-related encrustation. *J. Biomed. Mater. Res., Part B* **2006**, *76*, 1−7.

(65) Chow, K.; Dixon, J.; Gilpin, S.; Kavanagh, J. P.; Rao, P. N. Citrate inhibits growth of residual fragments in an in vitro model of calcium oxalate renal stones. *Kidney Int.* **2004**, *65*, 1724−1730.

(66) Brown, P.; Ackermann, D.; Finlayson, B. Calcium oxalate dihydrate (weddellite) precipitation. *J. Cryst. Growth* **1989**, *98*, 285−292.

(67) Chutipongtanate, S.; Thongboonkerd, V. Systematic comparisons of artificial urine formulas for in vitro cellular study. *Anal. Biochem.* **2010**, *402*, 110−112.

(68) Lee, S. C.; Hutchinson, J. M. R.; Inn, K. G. W.; Thein, M. An intercomparison study of 237Np determination in artificial urine samples. *Health Phys.* **1995**, *68*, 350−358.

(69) Ipe, D. S.; Horton, E.; Ulett, G. C. The basics of bacteriuria: strategies of microbes for persistence in urine. *Front. Cell. Infect. Microbiol.* **2016**, *6*, 14.

(70) dos Santos, E. C.; Maggioni, G. M.; Mazzotti, M. Statistical Analysis and Nucleation Parameter Estimation from Nucleation Experiments in Flowing Microdroplets. *Cryst. Growth Des.* **2019**, *19*, 6159−6174.

(71) Lange, T.; Charton, S.; Bizien, T.; Testard, F.; Malloggi, F. OSTE+ for in situ SAXS analysis with droplet microfluidic devices. *Lab Chip* **2020**, *20*, 2990−3000.

(72) Ferreira, J.; Castro, F.; Rocha, F.; Kuhn, S. Protein crystallization in a droplet-based microfluidic device: Hydrodynamic analysis and study of the phase behaviour. *Chem. Eng. Sci.* **2018**, *191*, 232−244.

(73) Ogobuiro, I.; Tuma, F. *Physiology, renal*; 2019.

(74) Smith, H. W. *The kidney: structure and function in health and disease*; Oxford University Press: USA, 1951; Vol. *1*.

(75) Koeppen, B.; Stanton, B. Regulation of body fluid osmolality: Regulation of water balance. *Renal Physiology*; Elsevier: Philadelphia, 2013, 79, DOI: 10.1016/B978-0-323-08691-2.00005-3.

(76) Vize, P. D.; Woolf, A. S.; Bard, J. B. *The kidney: from normal development to congenital disease*; Elsevier, 2003.

(77) Tabeling, P. *Introduction to microfluidics*; OUP Oxford, 2005.

(78) Jiang, S.; ter Horst, J. H. Crystal nucleation rates from probability distributions of induction times. *Cryst. Growth Des.* **2011**, *11*, 256−261.

(79) Kacker, R.; Dhingra, S.; Irimia, D.; Ghatkesar, M. K.; Stankiewicz, A.; Kramer, H. J. M.; Eral, H. B. Multiparameter Investigation of laser-induced nucleation of supersaturated aqueous KCl solutions. *Cryst. Growth Des.* **2018**, *18*, 312−317.

(80) Devos, C.; Van Gerven, T.; Kuhn, S. A Review of Experimental Methods for Nucleation Rate Determination in Large-Volume Batch and Microfluidic Crystallization. *Cryst. Growth Des.* **2021**, *21*, 2541−2565.

(81) Hood, K. *Comprehensive Polymer Science and Supplements*; Elsevier London, 1996.

(82) Tudose, A. E.; Dumitrascu, I.; Dumitrascu, L.; Dimitriu, D. G.; Dorohoi, D. O. In *Methods for determining the linear birefringence of some inorganic uniax crystals*; AIP Conference Proceedings, AIP Publishing LLC, 2017; p 030007.

(83) Luqman, A.; Stanifer, J.; Siddiqui, O. M. A.; Naseer, A.; Wall, B. M. Calcium oxalate monohydrate crystals: a clue to ethylene glycol poisoning. *Am. J. Med. Sci.* **2011**, *341*, 338.

(84) Isotalo, P. A.; Lloyd, R. V. Presence of birefringent crystals is useful in distinguishing thyroid from parathyroid gland tissues. *Am. J. Surg. Pathol.* **2002**, *26*, 813−814.

(85) Tornos, C.; Silva, E.; El-Naggar, A.; Pritzker, K. Calcium oxalate crystals in breast biopsies. *Am. J. Surg. Pathol.* **1990**, *14*, 961−968.

(86) Streit, J.; Tran-Ho, L.-C.; Königsberger, E. Solubility of the three calcium oxalate hydrates in sodium chloride solutionsand urine-like liquors. *Monatsh. Chem./Chem. Mon.* **1998**, *129*, 1225−1236.

(87) Harshe, Y. M.; van Eijk, M. J.; Kleijn, C. R.; Kreutzer, M. T.; Boukany, P. E. Scaling of mixing time for droplets of different sizes traveling through a serpentine microchannel. *RSC Adv.* **2016**, *6*, 98812−98815.

(88) Ibis, F.; Yu, T. W.; Penha, F. M.; Ganguly, D.; Nuhu, M. A.; van der Heijden, A. E. D. M.; Kramer, H. J. M.; Eral, H. B. Nucleation kinetics of calcium oxalate monohydrate as a function of pH, magnesium, and osteopontin concentration quantified with droplet microfluidics. *Biomicrofluidics* **2021**, *15*, No. 064103.

(89) Qian, J.-y.; Li, X.-j.; Gao, Z.-x.; Jin, Z.-j. Mixing efficiency and pressure drop analysis of liquid-liquid two phases flow in serpentine microchannels. *J. Flow Chem.* **2019**, *9*, 187−197.

(90) Qian, J.-y.; Chen, M.-r.; Wu, Z.; Jin, Z.-j.; Sunden, B. Effects of a Dynamic Injection Flow Rate on Slug Generation in a Cross-Junction Square Microchannel. *Processes* **2019**, *7*, 765.

(91) Ottino, J. M.; Ottino, J. M. *The kinematics of mixing: stretching, chaos, and transport*; Cambridge university press, 1989; Vol. *3*.

(92) Frey-Wyssling, A. Crystallography of the two hydrates of crystalline calcium oxalate in plants. *Am. J. Bot.* **1981**, *68*, 130−141.

(93) Stoiber, R. E.; Morse, S. A. Uniaxial Crystal Optics. In *Crystal Identification with the Polarizing Microscope*; Springer, 1994; pp. 116−122.

(94) Georgiev, R. N.; Toscano, S. O.; Uspal, W. E.; Bet, B.; Samin, S.; van Roij, R.; Eral, H. B. Universal motion of mirror-symmetric microparticles in confined Stokes flow. *Proc. Natl. Acad. Sci.* **2020**, *117*, 21865−21872.

(95) Rehor, I.; van Vreeswijk, S.; Vermonden, T.; Hennink, W. E.; Kegel, W. K.; Eral, H. B. Biodegradable microparticles for simultaneous detection of counterfeit and deteriorated edible products. *Small* **2017**, *13*, 1701804.

(96) Daudon, M.; Letavernier, E.; Frochot, V.; Haymann, J.-P.; Bazin, D.; Jungers, P. Respective influence of calcium and oxalate urine concentration on the formation of calcium oxalate monohydrate or dihydrate crystals. *C. R. Chim.* **2016**, *19*, 1504−1513.

(97) Zhang, J.; Wang, L.; Zhang, W.; Putnis, C. V. Role of Hyperoxaluria/Hypercalciuria in Controlling the Hydrate Phase Selection of Pathological Calcium Oxalate Mineralization. *Cryst. Growth Des.* **2021**, *21*, 683−691.

(98) Ferrari, E. S.; Davey, R. J. Solution-mediated transformation of α to β L-glutamic acid: Rate enhancement due to secondary nucleation. *Cryst. Growth Des.* **2004**, *4*, 1061−1068.

(99) Wesson, J. A.; Worcester, E. M.; Wiessner, J. H.; Mandel, N. S.; Kleinman, J. G. Control of calcium oxalate crystal structure and cell adherence by urinary macromolecules. *Kidney Int.* **1998**, *53*, 952−957.

(100) Chen, Z.-H.; Ren, X.-L.; Zhou, H.-H.; Li, X.-D. The role of hyaluronic acid in biomineralization. *Front. Mater. Sci.* **2012**, *6*, 283−296.

(101) WESSON, J. A.; WORCESTER, E. M.; KLEINMAN, J. G. Role of anionic proteins in kidney stone formation: interaction between model anionic polypeptides and calcium oxalate crystals. *J. Urol.* **2000**, *163*, 1343−1348.